The Astrophysical Journal, 939:104 (14pp), 2022 November 10 https://doi.org/10.3847/1538-4357/ac8f47

Photometric Objects Around Cosmic Webs (PAC) Delineated in a Spectroscopic Survey. III. Accurate Measurement of Galaxy Stellar Mass Function with the Aid of Cosmological Redshift Surveys

Kun Xu[1], Y. P. Jing[1,2], and Hongyu Gao[1]
[1] Department of Astronomy, School of Physics and Astronomy, Shanghai Jiao Tong University, Shanghai, 200240, People's Republic of China; ypjing@sjtu.edu.cn
[2] Tsung-Dao Lee Institute, and Shanghai Key Laboratory for Particle Physics and Cosmology, Shanghai Jiao Tong University, Shanghai, 200240, People's Republic of China
Received 2022 July 25; revised 2022 August 27; accepted 2022 September 3; published 2022 November 10

Abstract

We present a novel method to accurately measure the galaxy stellar mass function (GSMF) based upon the Photometric objects Around Cosmic webs (PAC) method developed in our first paper (Paper I) of the series. The method allows us to measure the GSMF to a lower-mass end that is not accessible to the spectroscopic sample used in the PAC. Compared with Paper I, the current measurement of GSMF is direct and model independent. We measure the GSMFs in the redshift ranges of z_s[3] < 0.2, $0.2 < z_s < 0.4$, and $0.5 < z_s < 0.7$ down to stellar masses of $M_* = 10^{8.2}$, $10^{10.6}$, and $10^{10.6}\,M_\odot$, using the data from the Dark Energy Spectroscopic Instrument (DESI) Legacy Imaging Surveys and the spectroscopic samples of Slogan Digital Sky Survey (i.e., Main, LOWZ, and CMASS samples). Our results show that there is no evolution of GSMF from $z_s = 0.6$ to $z_s = 0.1$ for $M_* > 10^{10.6}\,M_\odot$, and that there is a clear upturn at $M_* \approx 10^{9.5}\,M_\odot$ toward smaller galaxies in the local GMSF at $z_s = 0.1$. We provide an accurate double Schechter fit to the local GSMF for the entire range of M_* and a table of our measurements at the three redshifts, which can be used to test theories of galaxy formation. Our method can achieve an accurate measurement of GSMF to the stellar mass limit where the spectroscopic sample is already highly incomplete (e.g., $\sim 10^{-3}$) for its target selection.

Unified Astronomy Thesaurus concepts: Galaxy abundances (574); Galaxy formation (595); Galaxy properties (615); Stellar mass functions (1612)

1. Introduction

Galaxy stellar mass function (GSMF) is one of the most crucial measurements for our understanding of galaxy evolution. The amplitude and shape of the GSMF encode vital information about the galaxy star formation and quenching mechanisms, and have been used to infer and constrain the galaxy formation models in many studies.

According to the shapes of the GSMFs of star-forming and quenched galaxies, Peng et al. (2010) provided a model that separates the mass and environment quenching of galaxies at the local universe. Combined with the cosmic star formation rate, Behroozi et al. (2013) used the GSMFs at $z_s = 0 \sim 8$ to constrain the star formation histories as a function of the halo mass. Moster et al. (2013) determined the evolution of the galaxy-halo mass relation (SHMR) with the GSMFs at $z_s = 0 \sim 4$. In many studies (Wang et al. 2006; Wang & Jing 2010; Yang et al. 2012; Xu et al. 2022; Gao et al. 2022), the GSMF is used to accurately model the galaxy-halo connection combined with the galaxy correlation functions. Moreover, hydrodynamic simulations (Schaye et al. 2015; Pillepich et al. 2018; Davé et al. 2019) and semi-analytic models (Somerville et al. 2008; Benson 2012; Henriques et al. 2020) are often calibrated and tested by the GSMF.

Therefore, accurately measuring the GSMFs at different redshifts is necessary for galaxy formation and evolution studies. In the past two decades, an enormous amount of effort has been invested to measure the GSMF using different surveys and methods.

At low redshift ($z_s < 0.1$), large spectroscopic surveys, in particular the Two Degree Field Galaxy spectroscopic survey (2dF-GRS; Colless et al. 2001), Slogan Digital Sky Survey (SDSS; York et al. 2000), and Galaxy and Mass Assembly (GAMA; Driver et al. 2011), are used to study the local GSMF down to $10^{8.0}\,M_\odot$ (Cole et al. 2001; Bell et al. 2003; Blanton et al. 2003; Baldry et al. 2008, 2012; Li & White 2009; Weigel et al. 2016; Driver et al. 2022). The GSMF is found to be well characterized by a double Schechter function. However, although the survey areas are large, the survey volumes are still limited due to the shallow survey depths. For example, as will be demonstrated in Figure 3 below, low-mass galaxies ($<10^{9.0}\,M_\odot$) are only complete to $z_s \approx 0.03$ in the SDSS Main sample. The massive galaxies are also very few for their small number density. Thus, there are large uncertainties in the GSMF in both the small- and large-mass ends.

At intermediate redshifts ($z_s < 1$), deeper spectroscopic surveys begin to dominate the GSMF studies (Faber et al. 2007; Pozzetti et al. 2007, 2010; Drory et al. 2009; Davidzon et al. 2013; Moustakas et al. 2013), such as the DEEP2 Galaxy spectroscopic survey (Davis et al. 2003), the Visible Multi-Object Spectrograph (VIMOS) Very Large Telescope (VLT) Deep Survey (VVDS; Le Fèvre et al. 2005), zCOSMOS (Lilly et al. 2007), The PRIsm MUlti-object Survey (PRIMUS; Coil et al. 2011), and the VIMOS Public Extragalactic spectroscopic survey (VIPERS; Garilli et al. 2014). The GSMF has been explored down to $10^{10.0}\,M_\odot$ using

[3] Throughout the paper, we use z_s for spectroscopic redshift, z for the z-band magnitude.

these surveys. However, despite the huge efforts, measuring low-mass objects is still very difficult, and stellar-mass-limited samples are usually very small. In addition, incompleteness should be considered with caution when measuring the GSMF with the spectroscopic samples. A few effects such as those of target selection, fiber collision, the target sampling rate, and the spectroscopic success rate should be carefully considered, and the derived GSMF is sensitive to the details of the corrections for the incompleteness. Large spectroscopic surveys, such as Baryon Oscillation Spectroscopic Survey (BOSS; Alam et al. 2015; Reid et al. 2016), are also used to study the GSMF at the massive end at intermediate redshifts (Maraston et al. 2013). Due to the effects mentioned above, Leauthaud et al. (2016) found that CMASS and LOWZ samples are still incomplete for massive galaxies ($>10^{11.3}\,M_{\odot}$). To derive the GSMF from BOSS, Guo et al. (2018) modeled the galaxy clustering and incompleteness simultaneously using the incomplete conditional stellar mass function (ICSMF) framework, and inferred the GSMF from the constrained SHMR. This method attempted to recover the incompleteness, but their result is model dependent.

Deep multiband photometric surveys, which are deeper and more complete in terms of galaxy populations, are also used to study the GSMF at intermediate and high redshifts. Combining the ground-based deep photometric surveys and Hubble Space Telescope (HST) near-IR imaging, many studies push the measurements of the GSMF to $z_s > 1$ (Fontana et al. 2006; Ilbert et al. 2013; Muzzin et al. 2013; Tomczak et al. 2014; Mortlock et al. 2015; Davidzon et al. 2017; Wright et al. 2018; Leja et al. 2020; McLeod et al. 2021; Shuntov et al. 2022). The survey areas of the deep multiband photometric surveys are even smaller ($1 \sim 2\,\mathrm{deg}^2$) than the deep spectroscopic surveys, as they require long exposure times to reach very faint sources and multiple bands from UV to IR to obtain relatively accurate photometric redshifts (photoz) for faint objects. Wide photometric surveys are usually not suitable for the GSMF studies due to the fewer observed bands and shallower depths. Therefore, the cosmic variance should be taken carefully into account when measuring the GSMF using deep photometric surveys, especially at the high-mass end. Moreover, although faint sources can be detected in photometric surveys, photometric redshifts used in the GSMF studies are usually trained with the spectroscopic data, which may not cover for very faint sources, and therefore have larger errors. These problems associated with the photometric redshifts will also introduce uncertainties in the GSMF.

Furthermore, studying the evolution of the GSMF using the measurements from different surveys (Behroozi et al. 2013; Moster et al. 2013) should be very cautious especially at the high-mass end, where the GSMF changes exponentially. Small systematics, such as those from photometric calibration, source extraction and modeling, incompleteness correction, and the stellar mass estimation method, can cause large differences in the GSMF.

In Xu et al. (2022, hereafter Paper I), on the basis of Wang et al. (2011), we developed a method named Photometric objects Around Cosmic webs (PAC) to estimate the excess surface density $\bar{n}_2 w_p$ of photometric objects with certain physical properties around spectroscopically identified sources, which can take full use of the spectroscopically and deeper photometric surveys. In Paper I and the second paper (Xu & Jing 2022), based on PAC measurements, we have studied the SHMR and the galaxy assembly bias of massive galaxies. Based on the SHMR, we predicted the GSMF, which is in good agreement with the observations from the literature. In this third paper, we will combine the PAC measurements of $\bar{n}_2 w_{\rm p}$ and the projected cross-correlation function $w_{\rm p}$ measured from the spectroscopic samples, and derive $\bar{n}_2$, the GSMF in the photometric survey. The measurements of $w_{\rm p}$ are insensitive to the incompleteness of the spectroscopic samples in the galaxy stellar mass, once the sample can be used to accurately measure the projected cross-correlation function $w_{\rm p}$ (which is usually the case for cosmological redshift surveys). With this method, we can extend the study of GSMF to the lower-mass end with the wide spectroscopic and deeper photometric surveys. We can also provide measurements of the GSMFs in a uniform way (e.g., the same photometric catalog, the same stellar mass method) to redshift $z_s = 0.6$, which is better for evolution studies. Compared with the model prediction of GSMF in Paper I, the current measurement of GSMF is direct and model independent.

We introduce our method in Section 2. In Section 3, we describe the data and designs used to measure the GSMF. The results are shown in Section 4, and our conclusion is given in Section 5. We adopt the cosmology with $\Omega_m = 0.268$, $\Omega_\Lambda = 0.732$, and $H_0 = 71\,\mathrm{km\,s^{-1}\,Mpc^{-1}}$ throughout the paper.

2. Methodology

2.1. Photometric Objects Around Cosmic Webs (PAC)

Within a relatively narrow redshift range, suppose we want to study two types of galaxies with pop_1 from a spectroscopic catalog and pop_2 from a deep photometric catalog. In Paper I, we provide a method called PAC that can measure the excess projected density distribution $\bar{n}_2 w_{\rm p}(r_{\rm p})$ of pop_2 with certain physical properties around pop_1:

$$\bar{n}_2 w_{\rm p}(r_{\rm p}) = \frac{\bar{S}_2}{r_1^2} w_{12,\mathrm{weight}}(\theta), \tag{1}$$

where r_1 is the comoving distance to pop_1, $w_{\rm p}(r_{\rm p})$ and $w_{12,\mathrm{weight}}(\theta)$ are the projected cross-correlation function (PCCF) and the weighted angular cross-correlation function (ACCF) between pop_1 and pop_2 with $r_{\rm p} = r_1\theta$, and $\bar{n}_2$ and $\bar{S}_2$ are the mean number density and mean angular surface density of pop_2. As pop_1 has a redshift distribution, $w_{12}(\theta)$ is weighted by $1/r_1^2$ to account for the effect that $r_{\rm p}$ varies with redshift at fixed θ. The advantage of PAC is that it estimates the rest-frame physical properties of pop_2 statistically without the need of photoz, so that we can make full use of the deep photometric surveys. The main steps of PAC are:

1. Split pop_1 into narrower redshift bins, mainly accounting for the fast change in r_1 with the redshift.
2. Assuming all galaxies in pop_2 have the same redshift as the mean redshift in each redshift bin, calculate the physical properties of pop_2 using methods such as the spectral energy distribution (SED). Thus, in each redshift bin of pop_1, there is a physical property catalog of pop_2 .
3. In each redshift bin, select pop_2 with certain physical properties and by calculting $\bar{n}_2 w_{\rm p}(r_{\rm p})$ according to Equation (1). Foreground and background objects with wrong properties are canceled out through ACCF, and only pop_2 around pop_1 with correct redshifts are left.
4. Combine the results from different redshift bins by averaging with proper weights.

For more details, refer to Paper I.

2.2. Estimating the Galaxy Stellar Mass Function

Using PAC, we can calculate $\bar{n}_2 w_p(r_p)$ for pop_2 with certain stellar mass. We can also select a sample from the spectroscopic catalog with the same stellar mass. To distinguish these two samples, in the following, we denote the samples from the photometric catalog and the spectroscopic catalog as pop_2^p and pop_2^s, respectively. We can calculate the PCCF $w_p(r_p)$ between pop_1 and pop_2^s, and derive the number density $\bar{n}_2$ by comparing it to the PAC measurement $\bar{n}_2 w_p$.

The GSMF can be obtained by deriving $\bar{n}_2$ for pop_2 with different stellar masses. The low-mass end of the GSMF is still limited by the spectroscopic catalog, as the number of galaxies at the low-mass end may not even be enough to get $w_p(r_p)$.

With pop_1 and pop_2^s from spectroscopic catalogs at different redshifts and a deep photometric catalog, we can also measure the time evolution of the GSMF using PAC.

The whole process is straightforward and model independent with the only assumption that pop_2^s and pop_2^p have the same bias on large scales. According to the observed dependence (Li et al. 2006) of galaxy clustering on the color and the modeling predictions (Rodríguez-Puebla et al. 2015; Zu & Mandelbaum 2016), we find that the linear bias of blue (red) population is smaller (or larger) than the total population for $10^8 < M_* < 10^{11}\,M_\odot$ by < 0.1 dex, with the largest difference found at the smallest stellar mass. Therefore, our above assumption may lead an overestimate (underestimate) of the GSMF by the same amount if the population in the spectroscopic pop_2^s is dominated by blue (red) ones. This amount of systematics can be tolerated in the precision of our current measurement (see Figure 4). With the accuracy expected to improve in future surveys, the linear clustering bias of pop_2^s relative to pop_2^p should be carefully modeled.

3. Data and Designs

In this section, we introduce the observational data used in this work, and the details of the PAC and w_p measurements. Systematic errors and incompleteness of photometric and spectroscopic data are also carefully considered.

3.1. Photometric Data

We use the photometric catalogs[4] from the data release (DR) 9 of Dark Energy Spectroscopic Instrument (DESI) Legacy Imaging Surveys (Dey et al. 2019) throughout the paper. They cover over 14,000 deg^2 of the sky in the DESI (DESI Collaboration et al. 2016) footprint and consist of three different components:

1. The Dark Energy Camera Legacy Survey (DECaLS), which observes around 9000 deg^2 in both the Northern and Southern Galactic caps (NGC and SGC) at decl. $\leqslant 32$ deg in the g, r, and z bands. It also includes the data from the deeper Dark Energy Survey (DES; Dark Energy Survey Collaboration et al. 2016) in the SGC covering around 5000 deg^2, where 1130 deg^2 is in the DESI footprint.
2. The Beijing-Arizona Sky Survey (BASS), which covers 5000 deg^2 in the NGC footprint at decl. $\geqslant 32^\circ$ in the g and r bands but is around 0.5 mag shallower than DECaLS. It also observes additional 500 deg^2 in the DECaLS footprint in order to understand and correct the systematic biases.
3. The Mayall z-band Legacy Survey (MzLS), which observes the same footprint as BASS in the NGC footprint at decl. $\geqslant 32^\circ$ in the z band. The z-band depth is comparable to DECaLS.

Altogether, they provide three-band (g, r, and z) photometric data over more than 14,000 deg^2 (with additional 5000 deg^2 from DES) with a 5σ point-source depth of $g = 24.9$, $r = 24.2$, and $z = 23.3$ for DECaLS and MzLS, but BASS is around 0.5 mag shallower.

The Legacy Surveys images are processed using `Tractor`[5] (Lang et al. 2016), a forward-modeling approach to perform source extraction on pixel-level data. The sources are modeled with parametric profiles convolved with a specific point-spread function (PSF), including a delta function for the point source, exponential law, de Vaucouleurs law, and a Sérsic profile. The sources are classified into six morphological types according to the best-fit models: point sources (PSF), round exponential galaxies, de Vaucouleurs profiles, normal exponential profiles, and Sérsic profiles.

We only use the footprints that have been observed at least once in all three bands and add a bright-star mask and a bad-pixel mask to the catalogs using the MASKBITS[6] provided by the Legacy Surveys. The photometric catalog is further selected to match the survey geometry of the spectroscopic data at each redshift. Galactic extinction is corrected for all the sources using the maps of Schlegel et al. (1998).

To reject stars, we exclude sources with PSF morphologies. However, while it can remove most of the stars, there are still some stellar objects with extended morphologies left, such as close binaries. Therefore, following DESI LRG target selection (Zhou et al. 2020), with $W1$-band data from the Wide-field Infrared Survey Explorer (WISE; Wright et al. 2010), we adopt color cuts in the $r - z$ versus $z - W1$ diagram to further remove the stellar objects. We adopt color cuts different from Zhou et al. (2020) to preserve more galaxies especially at low z_s. The color cuts are shown in Figure 1 with stars have

$$(z - W1 < 0.8 \times (r - z) - 1.0) \text{ AND } (r - z > 1.0). \quad (2)$$

We would like to point out that, as stars are not correlated with spectroscopic galaxies, our PAC results are insensitive to the color cuts, but these cuts help remove the stars when we use the photometric catalog with photoz in Section 4.2.

3.2. Spectroscopic Data

Spectroscopic catalogs used for PAC in this work are all from SDSS (York et al. 2000). We focus on three redshift bins $0 < z_s < 0.2$, $0.2 < z_s < 0.4$, and $0.5 < z_s < 0.7$ using data from the SDSS DR7 Main sample (Abazajian et al. 2009) and the SDSS-III BOSS DR12 LOWZ and CMASS samples (Alam et al. 2015; Reid et al. 2016), respectively.

The DR7 Main sample provides a spectroscopic galaxy catalog complete to a `Petrosian` (Petrosian 1976) magnitude limit of $r = 17.77$, which covers over 7500 deg^2 of the NGC. It also includes three stripes covering additional 532 deg^2 in the

[4] https://www.legacysurvey.org/dr9/catalogs/

[5] https://github.com/dstndstn/tractor

[6] https://www.legacysurvey.org/dr9/bitmasks/

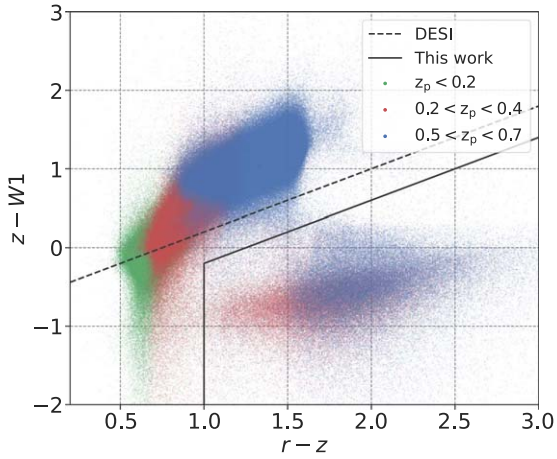

Figure 1. The $r-z$ vs. $z-W1$ color–color diagram for sources with $z<22.0$ from DECaLS color-coded according to their photometric redshift (Zhou et al. 2021). Dashed line is the nonstellar cut adopted in DESI LRG target selection (Zhou et al. 2020) and solid lines are the cuts adopted in this work.

SGC, which are not considered in this work. We use the "bright" Large Scale Structure (LSS) catalog[7] of the Main sample with collision corrections and a constant flux limit of $r<17.6$. We adopt a redshift cut of $z_s<0.2$ for the Main sample.

The LOWZ sample is designed to extend the SDSS-I/II Cut I LRG sample (Eisenstein et al. 2001) to $z_s\approx0.4$ and to fainter luminosities. It adopts a color–magnitude cut on galaxies with cmodel (Abazajian et al. 2004) brightness limits of $16<r<19.6$. We refer to Reid et al. (2016) for the full target selection strategy. We use the "LOWZ" LSS catalog[8] in BOSS DR12 for the LOWZ sample. The galaxies from the first nine months of the BOSS observation are excluded in the "LOWZ" catalog due to the incorrect star–galaxy separation criterion, resulting in a smaller footprint compared to "CMASS". In total, it covers 8337 deg^2 with 5836 deg^2 in the NGC and 2501 deg^2 in the SGC. We adopt a redshift cut of $0.2<z_s<0.4$ for the LOWZ sample.

The CMASS sample uses target selections similar to those of the SDSS-I/II Cut II LRG sample, but is bluer and fainter to increase the galaxy number density in the redshift range of $0.4<z_s<0.7$. Galaxies in the CMASS are selected with a number of magnitude and color cuts to get an approximately constant stellar mass. The cmodel magnitude limits for the CMASS sample are $17.6<i<19.9$, and the full selection criteria can be found in Reid et al. (2016). We use the "CMASS" LSS catalog in BOSS DR12 for the CMASS sample, which covers 9376 deg^2 of the sky with 6851 deg^2 in the NGC and 2525 deg^2 in the SGC. We adopt a redshift cut of $0.5<z_s<0.7$ for the CMASS sample.

All the three spectroscopic samples are within the footprint of the DESI Legacy Imaging Surveys. The spectroscopic sources are matched with the photometric catalog described above to get g-, r-, and z-band flux measurements.

3.3. Spectral Energy Distribution

Physical properties of the spectroscopic and photometric sources are estimated using the SED code CIGALE (Boquien et al. 2019) with the grz-band measurements.

We use the Bruzual & Charlot (2003) stellar population synthesis models with a Chabrier (2003) initial mass function and a delayed star formation history $\phi(t)\approx t\exp-t/\tau$. Three metallicities, $Z/Z_\odot=0.4$, 1, and 2.5, are considered, where $Z_\odot$ is the metallicity of the Sun. The Calzetti et al. (2000) extinction law with $0<E(B-V)<0.5$ is adopted for dust reddening. We use the bayes type of outputs from the CIGALE in this work.

3.4. Completeness and Designs

Despite the huge efforts of the survey teams, as shown in Appendix C, small but significant systematics still exist between the photometric measurements of DECaLS and BASS+MzLS, resulting in an offset in the stellar mass estimation. As shown in Appendix C, we use both DECaLS and BASS+MzLS for the w_p measurements and use only DECaLS for the PAC $\bar{n}_2 w_p$ measurements, because the offset has a much larger influence on $\bar{n}_2$ especially at the high-mass end, due to the exponential change in the GSMF.

Based on the test in Paper I, see Figure 3 there, we split both the LOWZ and CMASS samples into two narrower redshift bins with equal bin widths for the PAC measurements. As the comoving distance changes faster at the low redshifts, the Main sample is split into four redshift bins [0.05, 0.075], [0.075, 0.1], [0.1, 0.15], and [0.15, 0.2], and galaxies with $z_s<0.05$ are not used in the PAC measurements.

In the left panel of Figure 2, we show the stellar mass distribution of the three spectroscopic samples. According to the number of galaxies, we choose $[10^{8.1}, 10^{11.7}]\,M_\odot$, $[10^{10.5}, 10^{11.9}]\,M_\odot$, and $[10^{10.5}, 10^{12.1}]\,M_\odot$ as the stellar mass ranges of pop$_2$ for the Main sample, LOWZ, and CMASS, respectively, and split them into smaller mass bins with an equal logarithmic interval of 0.2 in $\log M_*$. They are also the stellar mass ranges we can calculate for the GSMFs at each redshift.

DECaLS is deep enough to reach $10^{10.5}\,M_\odot$ at the redshifts of LOWZ and CMASS (Paper I, see Figure 1). However, whether DECaLS is complete or not for $10^{8.1}\,M_\odot$ at $z_s<0.2$ remains to be explored. As in Paper I, we use the 10σ PSF depth as the depth for extended sources, which is more stringent than the galdepth provided by DECaLS. In the right panel of Figure 2, we show the cumulative distribution function (CDF) of the r-band 10σ PSF depth for DECaLS. We find that 90% of the regions in DECaLS are deeper than 23.15 mag. Thus, we use $r=23.15$ as the galaxy depth for DECaLS.

Deep photometric samples with photoz as used in Paper I are no longer suitable for completeness studies at $z_s<0.2$, as the survey volumes become too small and the photoz results in larger errors in the distance estimate. Instead, we use the deeper Galaxy And Mass Assembly (GAMA) DR4 spectroscopic sample (Driver et al. 2022), which covers around 250 deg^2 of the sky with a 95% completeness to $r_{\rm KiDS}=19.65$. The DR4 of GAMA replaced the previously used SDSS optical band ($ugri$) data with the much deeper Kilo Degree Survey (KiDS) DR4 data (Kuijken et al. 2019; Bellstedt et al. 2020), providing more reliable photometric measurements for the faint sources.

We calculate the stellar mass for galaxies in GAMA using SEDs and output the best-fit spectra. The spectra are redshifted to $z_s=0.075$, 0.1, 0.15, and 0.2 and are convolved with the DECaLS r-band filter to get the DECaLS r-band magnitudes, corresponding to the k corrections (Kinney et al. 1996; Blanton & Roweis 2007). We also calculate the $V_{\rm max}$ for each galaxy,

[7] http://sdss.physics.nyu.edu/lss/dr72/bright/
[8] https://data.sdss.org/sas/dr12/boss/lss/

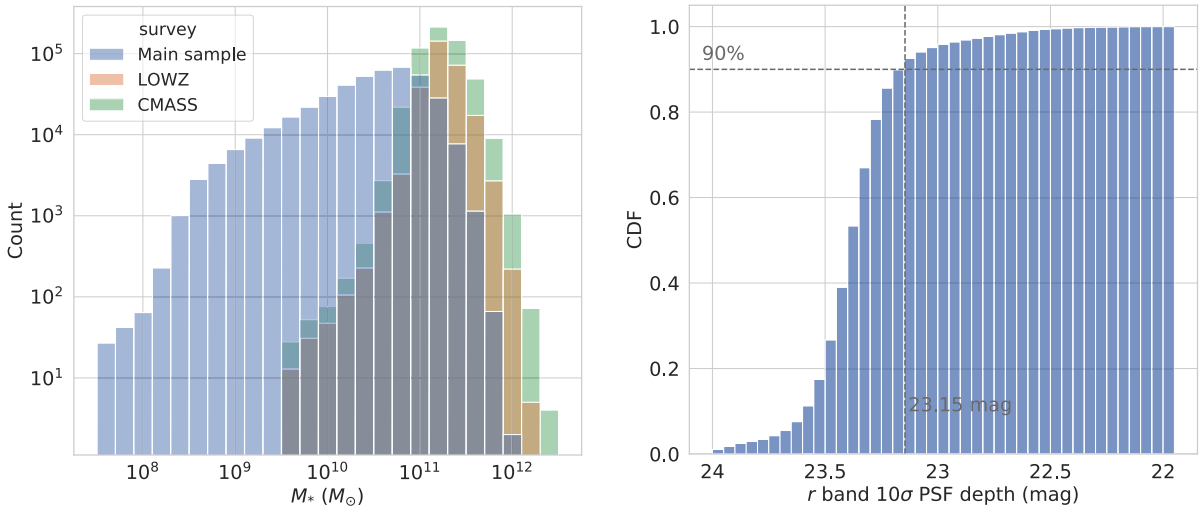

Figure 2. Left: stellar mass distributions for the Main, LOWZ and CMASS spectroscopic samples. Right: cumulative distribution function of the *r*band 10σ PSF depth for DECaLS.

where $V_{\rm max}$ is the volume corresponding to $z_{\rm max}$, the maximum redshift over which the galaxy can pass the GAMA selection criteria.

In Figure 3, we show the stellar mass—*k*-corrected *r*-band magnitude relations at four redshifts $z_s = 0.075$, 0.1, 0.15, and 0.2 for GAMA galaxies weight by $1/V_{\rm max}$. Following Paper I, we calculate the *r*-band completeness limit $C_{95}(M_*)$ that 95% of the galaxies are brighter than $C_{95}(M_*)$ in the *r* band for a given stellar mass M_* (red lines). For DECaLS with an *r*-band galaxy depth of 23.15 mag, the complete stellar masses are $10^{7.61}\,M_\odot$, $10^{7.89}\,M_\odot$, $10^{8.31}\,M_\odot$, and $10^{8.61}\,M_\odot$ at redshift 0.075, 0.1, 0.15, and 0.2 (gray dashed lines), respectively. Thus, for the Main sample, $\bar{n}_2 w_{\rm p}$ is only calculated at $z_s < 0.1$ and $z_s < 0.15$ for $\rm pop_2$ with mass of $10^{8.2}\,M_\odot$ and $10^{8.4}\,M_\odot$, and the whole redshift range is used for $\rm pop_2$ larger than $10^{8.6}\,M_\odot$.

Then, we choose the stellar mass range of $\rm pop_1$ as $[10^{10.3}, 10^{11.3}]\,M_\odot$ for the Main sample and $[10^{11.3}, 10^{11.9}]\,M_\odot$ for LOWZ and CMASS. To check the systematics of the data and our method, we also split $\rm pop_1$ into several stellar mass bins with an equal logarithmic interval of 0.2. However, when cross-correlating with $\rm pop_2$ of the smallest or largest mass bin, it is hard to calculate $w_{\rm p}$ if the $\rm pop_1$ sample is divided as stated previously. In these cases, the whole spectroscopic samples are used.

The final designs for the measurements of $w_{\rm p}$ and $\bar{n}_2 w_{\rm p}$ are summarized in Table 1.

3.5. Measurements of $\bar{n}_2 w_{\rm p}$, $\rm w_p$, and $\bar{n}_2$

For a particular mass and redshift bin of $\rm pop_2^p$ and $\rm pop_1$, $\bar{n}_2 w_{\rm p}$ is calculated in a few narrower redshift subbins for two separate regions (DECaLS NGC and DECaLS SGC), and then the results are combined. To properly account for the contributions from different redshift bins and from the two regions, we consider a more refined method than in Paper I to combine the $\bar{n}_2 w_{\rm p}$ results.

Let $\mathcal{A} \equiv \bar{n}_2 w_{\rm p}$ for better representation. Assuming $\mathcal{A}$ is calculated in $N_{\rm r}$ narrower redshift bins and $N_{\rm s}$ sky regions, we further split each sky region into $N_{\rm sub}$ subregions for error estimation using jackknife resampling. $\mathcal{A}_{i,j,k}$ can be calculated according to Equation (1) in the *i*th redshift bin, *j*th sky region, and *k*th jackknife subsamlpe. Measurements from different sky regions are first combined, weighted by the areas $w_{\rm s}$ of the regions:

$$\mathcal{A}_{i,k} = \frac{\sum_{j=1}^{N_{\rm s}} \mathcal{A}_{i,j,k} w_{{\rm s},j}}{\sum_{j=1}^{N_{\rm s}} w_{{\rm s},j}}. \tag{3}$$

Then, we estimate the mean values and the uncertainties of the mean values for each redshift bins from $N_{\rm sub}$ subsamples:

$$\mathcal{A}_i = \sum_{k=1}^{N_{\rm sub}} \mathcal{A}_{i,k} / N_{\rm sub}, \tag{4}$$

$$\sigma^2_{\mathcal{A},i} = \frac{N_{\rm sub} - 1}{N_{\rm sub}} \sum_{k=1}^{N_{\rm sub}} (\mathcal{A}_{i,k} - \mathcal{A}_i)^2. \tag{5}$$

Finally, results from different redshift bins are combined according to the uncertainties

$$\mathcal{A} = \frac{\sum_{i=1}^{N_{\rm r}} \mathcal{A}_i / \sigma^2_{\mathcal{A},i}}{\sum_{i=1}^{N_{\rm r}} 1 / \sigma^2_{\mathcal{A},i}}, \tag{6}$$

$$\sigma^2_{\mathcal{A}} = \frac{1}{\sum_{i=1}^{N_{\rm r}} 1 / \sigma^2_{\mathcal{A},i}}. \tag{7}$$

Using the spectroscopic samples $\rm pop_2^s$ and $\rm pop_1$, $w_{\rm p}$ and $\sigma_{w_{\rm p}}$ can be calculated in the same way. However, the samples are not split into narrower redshift bins as done in PAC, so the final step can be ignored or you may regard $N_{\rm r} = 1$. $w_{\rm p}$ is estimated using the Landy–Szalay estimator (Landy & Szalay 1993).

$\mathcal{A}$ and $w_{\rm p}$ estimated above are only used for the tests of systematics and verification of modeling. We do not use the simple error propagation to calculate the $\bar{n}_2$ and its uncertainty. Instead, we use a more sophisticated way. After we combine the measurements from different sky regions and obtain $\mathcal{A}_{i,k}$ and $w_{{\rm p},k}$, we can calculate $\bar{\boldsymbol{n}}_{2,i,k}$ in different radial bins:

$$\bar{\boldsymbol{n}}_{2,i,k} = \mathcal{A}_{i,k} / w_{{\rm p},k}. \tag{8}$$

The $N_{\rm sub}$ $\bar{n}_2$ arrays in the same redshift bins are assumed to have the same statistical power, so we can calculate the mean value and covariance matrices for the $\bar{n}_2$ arrays in each redshift:

$$\bar{\boldsymbol{n}}_{2,i} = \sum_{k=1}^{N_{\rm sub}} \bar{\boldsymbol{n}}_{2,i,k} / N_{\rm sub}, \tag{9}$$

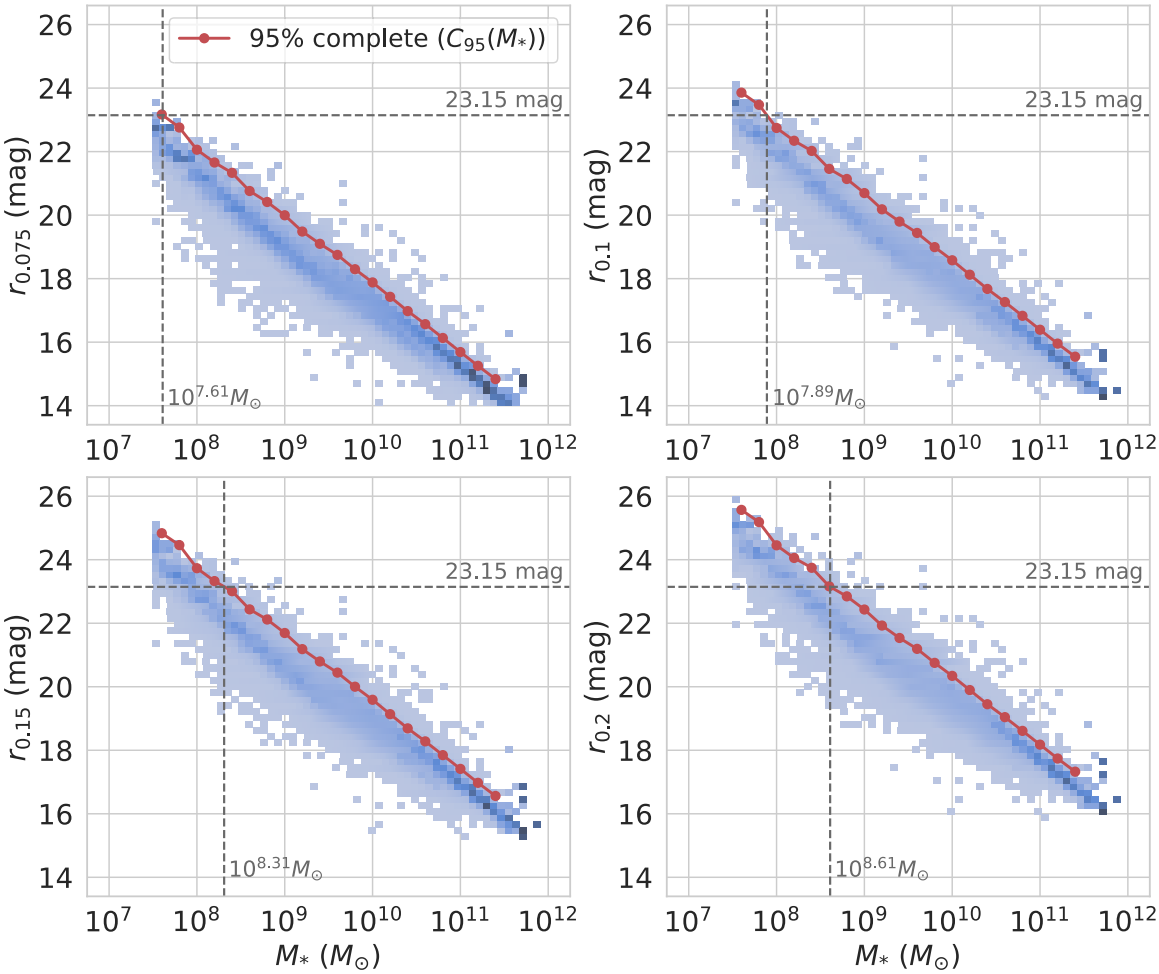

Figure 3. Stellar mass–r band magnitude relations for GAMA DR4 galaxies k-corrected to $z_s = 0.075$, 0.1, 0.15, and 0.2. Galaxies are weighted by $1/V_{\rm max}$. Red lines with dots show the 95% completeness limits $C_{95}(M_*)$ varying with the stellar mass at each redshifts. Gray dashed lines show the stellar mass limits for DECLaS with an r-band depth of 23.15 mag.

Table 1
Final Designs for the $w_{\rm p}$ (DECLaS and BASS+MzLS) and PAC (DECaLS) Measurements

Redshift	Survey	pop$_1$[a] ($M_\odot$)	pop$_2$[b] ($M_\odot$)	PAC Redshift Bins
[0, 0.2]	Main	[$10^{10.3}$, $10^{11.3}$]	[$10^{8.1}$, $10^{11.7}$]	[0.05, 0.075], [0.075, 0.1], [0.1, 0.15], [0.15, 0.2]
[0.2,0.4]	LOWZ	[$10^{11.3}$, $10^{11.9}$]	[$10^{10.5}$, $10^{11.9}$]	[0.2, 0.3], [0.3, 0.4]
[0.5,0.7]	CMASS	[$10^{11.3}$, $10^{11.9}$]	[$10^{10.5}$, $10^{12.1}$]	[0.5, 0.6], [0.6, 0.7]

Notes.
[a] Stellar mass ranges of pop$_1$ with an fiducial equal logarithmic bin width of $10^{0.2}\,M_\odot$.
[b] Stellar mass ranges of pop$_2$ with an fiducial equal logarithmic bin width of $10^{0.2}\,M_\odot$.

$$C_{ab,i} = \frac{N_{\rm sub}-1}{N_{\rm sub}}\sum_{k=1}^{N_{\rm sub}}(\bar{n}^a_{2,i,k}-\bar{n}^a_{2,i})(\bar{n}^b_{2,i,k}-\bar{n}^b_{2,i}), \quad (10)$$

where a and b denote the ath and bth radial bins. We define the χ^2 as:

$$\chi^2 = \sum_{i=1}^{N_{\rm r}}(\bar{\boldsymbol{n}}_{2,i}-\bar{n}_2)^T\boldsymbol{C}^{-1}(\bar{\boldsymbol{n}}_{2,i}-\bar{n}_2), \quad (11)$$

where $\bar{n}_2$ is a constant to be determined, $\boldsymbol{C}^{-1}$ is the inverse of $\boldsymbol{C}$, and T denotes matrix transposition.

We further split pop$_1$ into $N_{\rm m}$ mass bins. In principle, $\bar{n}_2$ from different pop$_1$ mass bins should be the same. Comparing the fittings in different mass bins can give a consistency check of the data and method, although this may not be done in the smallest mass bins where the numbers of galaxies are too few. So the final $\chi^2_{\rm all}$ is defined as:

$$\chi^2_{\rm all} = \sum_{m=1}^{N_{\rm m}}\chi^2_{\rm m}, \quad (12)$$

where $\chi^2_{\rm m}$ is the χ^2 for the mth pop$_1$ mass bin. We use the Markov chain Monte Carlo (MCMC) sampler `emcee`

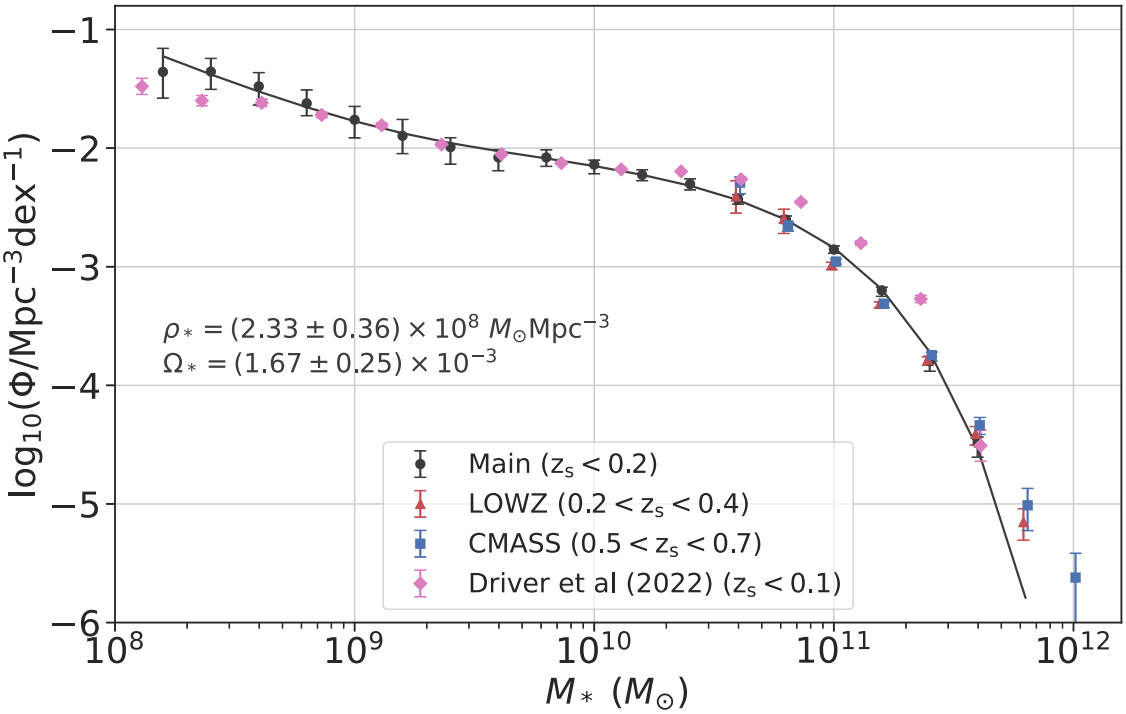

Figure 4. GSMFs estimated according to the designs in Table 1 using the Main sample ($z_s < 0.2$, black), LOWZ ($0.2 < z_s < 0.4$, red), and CMASS ($0.5 < z_s < 0.7$, blue). The results from the Main sample are fitted by a double Schechter function shown in black line. The GAMA DR4 (Driver et al. 2022) measurements are provided for comparison and shown with purple diamonds. The GSFD (ρ_* and Ω_*) from the Main sample results is also given.

(Foreman-Mackey et al. 2013) to perform a maximum likelihood analysis of $\{\bar{n}_2\}$.

4. Results

In this section, we present the GSMF measurements for the three redshift ranges.

4.1. Galaxy Stellar Mass Functions

We estimate $\bar{n}_2$ at different stellar masses to get the GSMFs for the three redshift ranges according to the designs in Table 1. For every mass bin, w_p and $\mathcal{A}$ are calculated in the radial range of $0.1h^{-1}\mathrm{Mpc} < r_p < 15h^{-1}\mathrm{Mpc}$ with $N_{\rm sub} = 100$.

Comparisons between w_p and the modeled $\mathcal{A}/\bar{n}_2$ for different mass bins of pop_1 and pop_2 are shown in Figures A1, A2, and A3 for the Main sample, LOWZ, and CMASS, respectively. Results for the same pop_2 from different pop_1 masses are consistent with each other, confirming that our methods and results are reliable. Moreover, in the Main sample, w_p and $\mathcal{A}/\bar{n}_2$ do not vary with the pop_2 mass at the low-mass end ($<10^{10.0}\,M_\odot$), which is in good agreement with the expected nearly constant bias for small galaxies (halos; Jing 1998; Peacock & Smith 2000; Tinker et al. 2010; Desjacques et al. 2018).

The GSMFs for the three redshift ranges are shown in Figure 4 and are also listed in Table B1. At the high-mass end ($>10^{10.6}\,M_\odot$), which is covered by three redshifts, the GSMF shows nearly no evolution with the redshift. From the low-redshift results of the Main sample, our measurements confirm an upturn and a steepening at the low-mass end of the GSMF, which has been reported in some previous studies (Popesso et al. 2006; Baldry et al. 2008; Tinker et al. 2010; Baldry et al. 2012; McLeod et al. 2021; Driver et al. 2022).

Table 2
Parameters of the Double Schechter Function for the GSMF from the Main Sample ($z_s < 0.2$)

$\log_{10}\phi_0$ (Mpc^{-3})	$\log_{10}M_1$ ($M_\odot$)	$\log_{10}M_2$ ($M_\odot$)	α_1	α_2
$-13.58^{+0.24}_{-0.31}$	$10.92^{+0.11}_{-0.09}$	$9.18^{+0.57}_{-0.57}$	$-1.22^{+0.15}_{-0.15}$	$-1.97^{+0.90}_{-0.87}$

To characterize the upturn structure, we fit the GSMF at the low redshift with a double Schechter function with five parameters (Popesso et al. 2006):

$$\phi(M_*)dM_* = \phi_0\left[\left(\frac{M_*}{M_1}\right)^{\alpha_1}\exp\left(-\frac{M_*}{M_1}\right) + \left(\frac{M_1}{M_2}\right)\left(\frac{M_*}{M_2}\right)^{\alpha_2}\exp\left(-\frac{M_*}{M_2}\right)\right]dM_*, \quad (13)$$

where $\phi(M_*)dM_*$ is the number density of galaxies with mass between M_* and $M_* + dM_*$. We always choose $M_1 > M_2$ such that the second term dominates at lower masses. As the number density Φ we measured is in an equal logarithmic interval, we have

$$\Phi(M_*) = \ln(10)M_*\phi(M_*). \quad (14)$$

The best-fit double Schechter function is shown in Figure 4 with a black line, with the parameters listed in Table 2.

The galaxy stellar mass density (GSMD) can be obtained by integrating over the GSMF. We report a GSMD of $\rho_* = (2.33 \pm 0.36) \times 10^8\,M_\odot\,\mathrm{Mpc}^{-3}$ and $\Omega_* = \rho_*/\rho_{\rm crit} = (1.67 \pm 0.25) \times 10^{-3}$ at $z_s < 0.2$ from our measurements, with an upper limit of $10^{12.5}\,M_\odot$ and a lower limit of $10^{6.0}\,M_\odot$ for the integration.

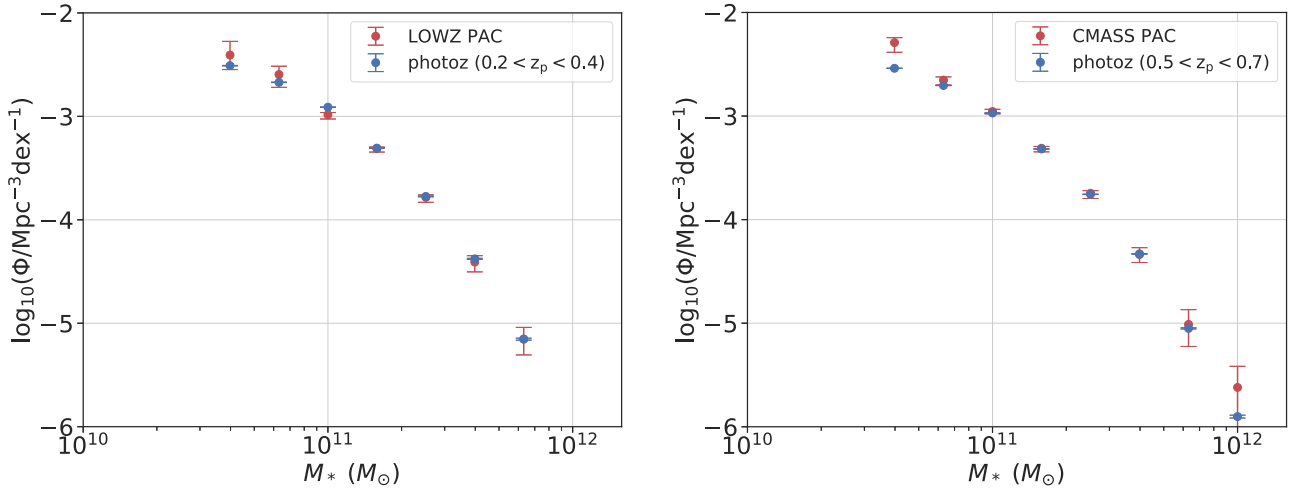

Figure 5. Comparisons of the GSMFs from PAC (red) and DECaLS photoz (blue; Zhou et al. 2021) at the massive ends for the LOWZ (left; $0.2 < z_p < 0.4$) and CMASS (right; $0.5 < z_p < 0.7$) redshift ranges.

The GSMF from GAMA DR4 (Driver et al. 2022) at $z_s < 0.1$ is also shown in Figure 4 for comparison. We find that for $10^9 < M_* < 10^{10}\,M_\odot$, their measurement agrees with ours almost perfectly. However, at higher masses, their GSMF is higher than ours by < 0.3 dex, while at lower masses, our GSMF is higher. The reason for the discrepancies is not fully understood, especially for the range of $10^{10.3} < M_* < 10^{11.3}\,M_\odot$. For the lowest stellar mass $M_* < 10^9 M_\odot$, the volume surveyed by GAMA is much smaller and our measurements show a slightly steeper upturn.

4.2. Comparisons with Photometric Redshift

For a survey like DECaLS, the photometric redshift can be measured accurately at the bright end and at intermediate redshifts ($z_s \sim 0.5$) as shown in many studies (Moutard et al. 2016; Zhou et al. 2021; Newman & Gruen 2022), as there are enough spectroscopically identified galaxies covering the whole galaxy population for training, the photometric magnitudes are accurate, and the important spectral features like the 4000 Å break are well sampled.

To verify whether photozs from the wide photometric surveys are reliable for the GSMF study, we calculate the stellar mass for the DECaLS galaxies using the photoz from Zhou et al. (2021) estimated using the DECaLS and WISE (Wright et al. 2010) photometry. We compare the GSMFs from the PAC and photoz measurements in Figure 5 for the LOWZ ($0.2 < z_p < 0.4$) and CMASS ($0.5 < z_p < 0.7$) redshift ranges. Errors of the GSMFs from photoz are estimated using jackknife resampling. We also list the measurements from photoz in Table B1.

The two independent measurements from PAC and photoz are in excellent agreement with each other in both redshift ranges at least for $M_* > 10^{11.0}\,M_\odot$. Although for $M_* = 10^{12.0}\,M_\odot$ in the CMASS redshift range the mean value from PAC is higher than that from photoz, the error of PAC in this mass bin is large. This consistency confirms both that our PAC method for GSMF measurements is reliable and that photoz from wide photometric surveys estimated from only a few bands is suitable for GSMF studies at intermediate redshifts ($0.2 < z_p < 0.7$) and massive ends ($M_* > 10^{11.0}\,M_\odot$). Thus, we verify that photoz are suitable for LRG target selection and mass completeness studies (Leauthaud et al. 2016; Zhou et al. 2020; K. Xu et al. 2022, in preparation).

5. Conclusion

In this paper, we provide a model-independent method for measuring the GSMF by combining the PAC measurements of $\bar{n}_2 w_\mathrm{p}$ and spectroscopic measurements of w_p. We apply this method to the photometric catalog from the DESI Legacy Imaging Surveys and the spectroscopic catalogs from the SDSS Main sample ($z_s < 0.2$), LOWZ sample ($0.2 < z_s < 0.4$), and CMASS sample ($0.5 < z_s < 0.7$), and obtain the GSMFs at the three redshifts down to $10^{8.2}\,M_\odot$, $10^{10.6}\,M_\odot$, and $10^{10.6}\,M_\odot$, respectively.

At the high-mass end ($>10^{10.6}\,M_\odot$), our measurement shows that there is no evolution of GSMF as $z_s = 0.6$. At the low-mass end ($<10^{9.0}\,M_\odot$), we find an upturn in the GSMF at $z_s < 0.2$, which is slightly steeper than reported in Driver et al. (2022) using the GAMA DR4 data. We also report a galaxy stellar mass density (GSMD) of $\rho_* = (2.33 \pm 0.36) \times 10^8\,M_\odot \mathrm{Mpc}^{-3}$ and $\Omega_* = (1.67 \pm 0.25) \times 10^{-3}$ at $z_s < 0.2$.

We compare the PAC measurements of the GSMFs with the DECaLS photoz measurements and find that the two results are in excellent agreement with each other at intermediate redshifts ($0.2 < z_p < 0.7$) and massive ends ($M_* > 10^{11.0}\,M_\odot$), verifying both that our method is reliable and photoz is also suitable for LRG target selection and mass completeness studies. The accurate measurements of the GSMFs for $z_s < 0.7$ also provide a test bed for semi-analytical models and hydrodynamical simulations of galaxy formation.

Our result also shows that our method can achieve a relatively good measurement of GSMF with a spectroscopic sample that is even highly incomplete ($\sim 10^{-3}$) in stellar mass (see the results for the LOWZ and CMASS samples). With our method, spectroscopic surveys with low target sampling rates can also be useful for GSMF studies.

With the next generation large and deep photometric and spectroscopic surveys such as DESI (DESI Collaboration et al. 2016), Legacy Survey of Space and Time (Ivezić et al. 2019) and Euclid (Laureijs et al. 2011), we can extend the GSMF measurements to higher redshifts and smaller stellar masses.

The work is supported by NSFC (12133006, 11890691, 11621303) and by 111 project No. B20019. We gratefully acknowledge the support of the Key Laboratory for Particle Physics, Astrophysics and Cosmology, Ministry of Education. This work made use of the Gravity Supercomputer at the Department of Astronomy, Shanghai Jiao Tong University.

This publication has made use of data products from the Sloan Digital Sky Survey (SDSS). Funding for SDSS and SDSS-II has been provided by the Alfred P. Sloan Foundation, the Participating Institutions, the National Science Foundation, the U.S. Department of Energy, the National Aeronautics and Space Administration, the Japanese Monbukagakusho, the Max Planck Society, and the Higher Education Funding Council for England.

Funding for SDSS-III has been provided by the Alfred P. Sloan Foundation, the Participating Institutions, the National Science Foundation, and the U.S. Department of Energy Office of Science. The SDSS-III website is http://www.sdss3.org/. SDSS-III is managed by the Astrophysical Research Consortium for the Participating Institutions of the SDSS-III Collaboration including the University of Arizona, the Brazilian Participation Group, Brookhaven National Laboratory, Carnegie Mellon University, University of Florida, the French Participation Group, the German Participation Group, Harvard University, the Instituto de Astrofisica de Canarias, the Michigan State/Notre Dame/JINA Participation Group, Johns Hopkins University, Lawrence Berkeley National Laboratory, Max Planck Institute for Astrophysics, Max Planck Institute for Extraterrestrial Physics, New Mexico State University, New York University, Ohio State University, Pennsylvania State University, University of Portsmouth, Princeton University, the Spanish Participation Group, University of Tokyo, University of Utah, Vanderbilt University, University of Virginia, University of Washington, and Yale University.

The Legacy Surveys consist of three individual and complementary projects: the Dark Energy Camera Legacy Survey (DECaLS; Proposal ID #2014B-0404; PIs: David Schlegel and Arjun Dey), the Beijing-Arizona Sky Survey (BASS; NOAO Prop. ID #2015A-0801; PIs: Zhou Xu and Xiaohui Fan), and the Mayall z-band Legacy Survey (MzLS; Prop. ID #2016A-0453; PI: Arjun Dey). DECaLS, BASS and MzLS together include data obtained, respectively, at the Blanco telescope, Cerro Tololo Inter-American Observatory, NSF's NOIRLab; the Bok telescope, Steward Observatory, University of Arizona; and the Mayall telescope, Kitt Peak National Observatory, NOIRLab. The Legacy Surveys project is honored to be permitted to conduct astronomical research on Iolkam Du'ag (Kitt Peak), a mountain with particular significance to the Tohono O'odham Nation.

Appendix A
Measurements and Fittings

In Figures A1, A2, and A3, we check the modeling results of $\bar{n}_2$ by comparing $\mathcal{A}/\bar{n}_2$ with w_p for the Main sample, LOWZ, and CMASS, respectively. Dots with error bars show the results for w_p, and lines with shadows are the results for $\mathcal{A}/\bar{n}_2$. Each panel show the results for the same mass bin of pop_2 and different colors are for different mass bins of pop_1. In all mass bins, $\mathcal{A}/\bar{n}_2$ is in good agreement with w_p, confirming that our methods and results are robust and reliable.

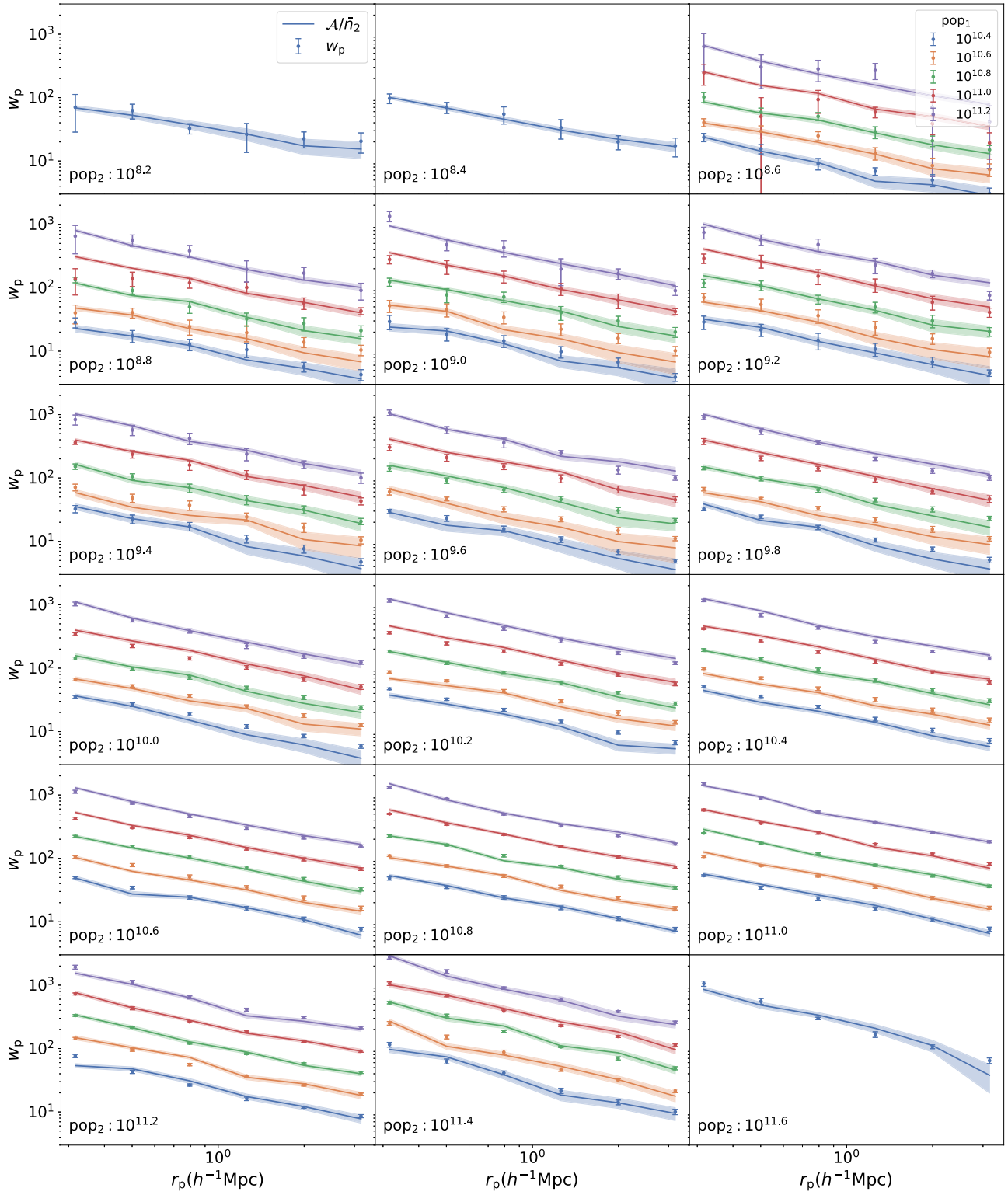

Figure A1. Comparing $\mathcal{A}/\bar{n}_2$ (lines) with w_p (dots) for the Main sample. Each panel is for the same mass bin of pop$_2$. Different colors are for different mass bins of pop$_1$, and results are multiplied by 0.25, 0.5, 1, 2, and 4 for better illustration.

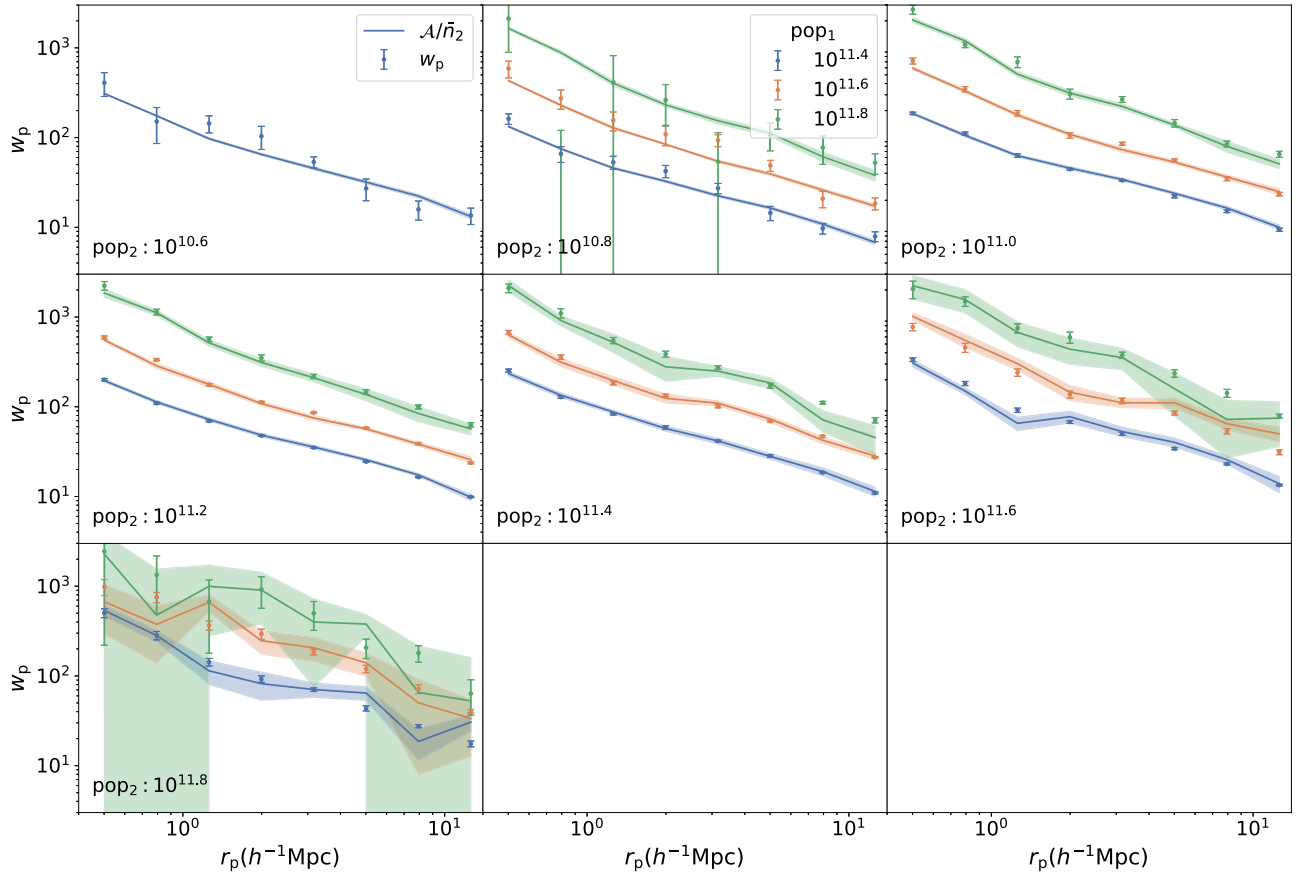

Figure A2. The same as Figure A1 but for LOWZ.

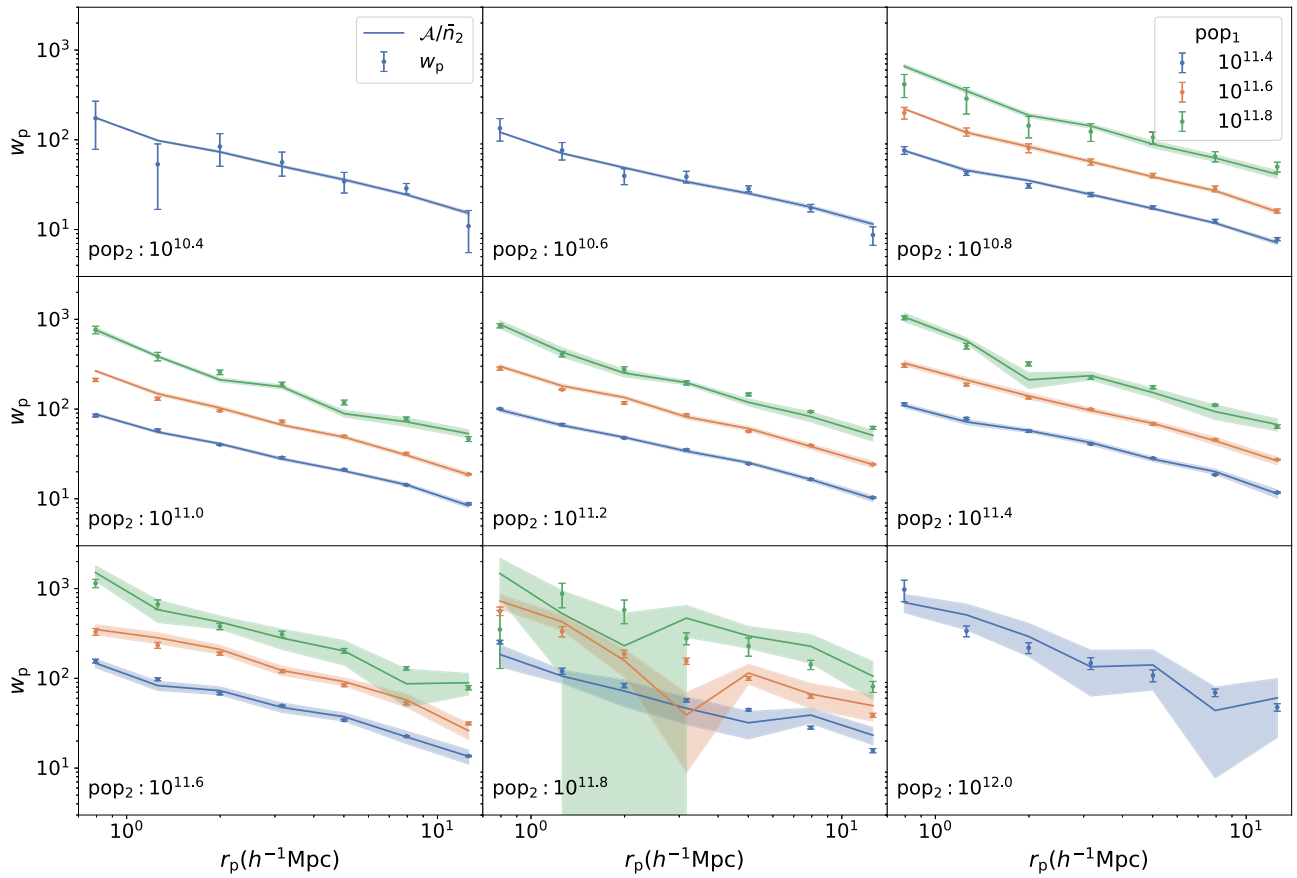

Figure A3. The same as Figure A1 but for CMASS.

Appendix B
The GSMFs in Tabular Form

In Table B1, we list the mean values and errors of the estimated GSMFs $\log_{10}(\Phi/\mathrm{Mpc}^{-3}\,\mathrm{dex}^{-1})$ at different redshift ranges from both PAC (z_s) and DECaLS photoz (z_p).

Table B1
The Galaxy Stellar Mass Number-density Distributions $\log_{10}(\Phi/\mathrm{Mpc}^{-3}\,\mathrm{dex}^{-1})$ at Different Redshifts from PAC (z_s) and DECaLS photoz (z_p)

$\log_{10}(M_*/M_\odot)$	$z_s < 0.2$	$0.2 < z_s < 0.4$	$0.5 < z_s < 0.7$	$0.2 < z_p < 0.4$	$0.5 < z_p < 0.7$
8.2	$-1.36^{+0.20}_{-0.22}$				
8.4	$-1.35^{+0.11}_{-0.15}$				
8.6	$-1.47^{+0.12}_{-0.16}$				
8.8	$-1.62^{+0.11}_{-0.10}$				
9.0	$-1.76^{+0.11}_{-0.15}$				
9.2	$-1.90^{+0.14}_{-0.15}$				
9.4	$-1.99^{+0.08}_{-0.14}$				
9.6	$-2.08^{+0.07}_{-0.11}$				
9.8	$-2.08^{+0.06}_{-0.08}$				
10.0	$-2.14^{+0.04}_{-0.08}$				
10.2	$-2.23^{+0.04}_{-0.05}$				
10.4	$-2.30^{+0.04}_{-0.05}$				
10.6	$-2.43^{+0.04}_{-0.04}$	$-2.41^{+0.13}_{-0.14}$	$-2.29^{+0.05}_{-0.09}$	$-2.505^{+0.002}_{-0.002}$	$-2.538^{+0.001}_{-0.001}$
10.8	$-2.60^{+0.03}_{-0.03}$	$-2.60^{+0.08}_{-0.12}$	$-2.65^{+0.03}_{-0.05}$	$-2.667^{+0.002}_{-0.002}$	$-2.705^{+0.001}_{-0.001}$
11.0	$-2.85^{+0.03}_{-0.03}$	$-2.98^{+0.02}_{-0.04}$	$-2.96^{+0.02}_{-0.02}$	$-2.905^{+0.002}_{-0.002}$	$-2.970^{+0.001}_{-0.001}$
11.2	$-3.20^{+0.03}_{-0.05}$	$-3.31^{+0.02}_{-0.03}$	$-3.31^{+0.02}_{-0.03}$	$-3.298^{+0.003}_{-0.003}$	$-3.318^{+0.002}_{-0.002}$
11.4	$-3.80^{+0.04}_{-0.08}$	$-3.78^{+0.02}_{-0.05}$	$-3.75^{+0.03}_{-0.05}$	$-3.764^{+0.004}_{-0.004}$	$-3.756^{+0.002}_{-0.002}$
11.6	$-4.49^{+0.05}_{-0.12}$	$-4.41^{+0.06}_{-0.09}$	$-4.34^{+0.07}_{-0.08}$	$-4.366^{+0.005}_{-0.005}$	$-4.330^{+0.004}_{-0.004}$
11.8		$-5.15^{+0.11}_{-0.15}$	$-5.01^{+0.14}_{-0.21}$	$-5.141^{+0.009}_{-0.009}$	$-5.050^{+0.006}_{-0.006}$
12.0			$-5.61^{+0.20}_{-0.40}$		$-5.901^{+0.013}_{-0.014}$

Appendix C
Systematics between DECaLS and BASS+MzLS

In Figure C1, we compare the w_p and $\bar{n}_2 w_p$ measurements from the DECaLS samples alone and the full DECaLS+BASS +MzLS samples, with pop_1 of $10^{10.8}\,M_\odot$ and pop_2 of $10^{11.4}\,M_\odot$ at $z_s < 0.2$. As shown in the figure, there are both systematics in the measurements of w_p and $\bar{n}_2 w_p$ for the two samples, but the relative offset is much smaller in $w_p (< 10\%)$ than in $\bar{n}_2 w_p (> 20\%)$, which may due to the much faster changes in GSMF with the stellar mass than galaxy bias at the high-mass end. Thus, we decide to use both DECaLS and BASS+MzLS for the w_p measurements, while use only DECaLS for the PAC measurements. In this way, we can reduce the statistical uncertainties in the measurements of w_p and avoid the large systematics from the measurements $\bar{n}_2 w_p$.

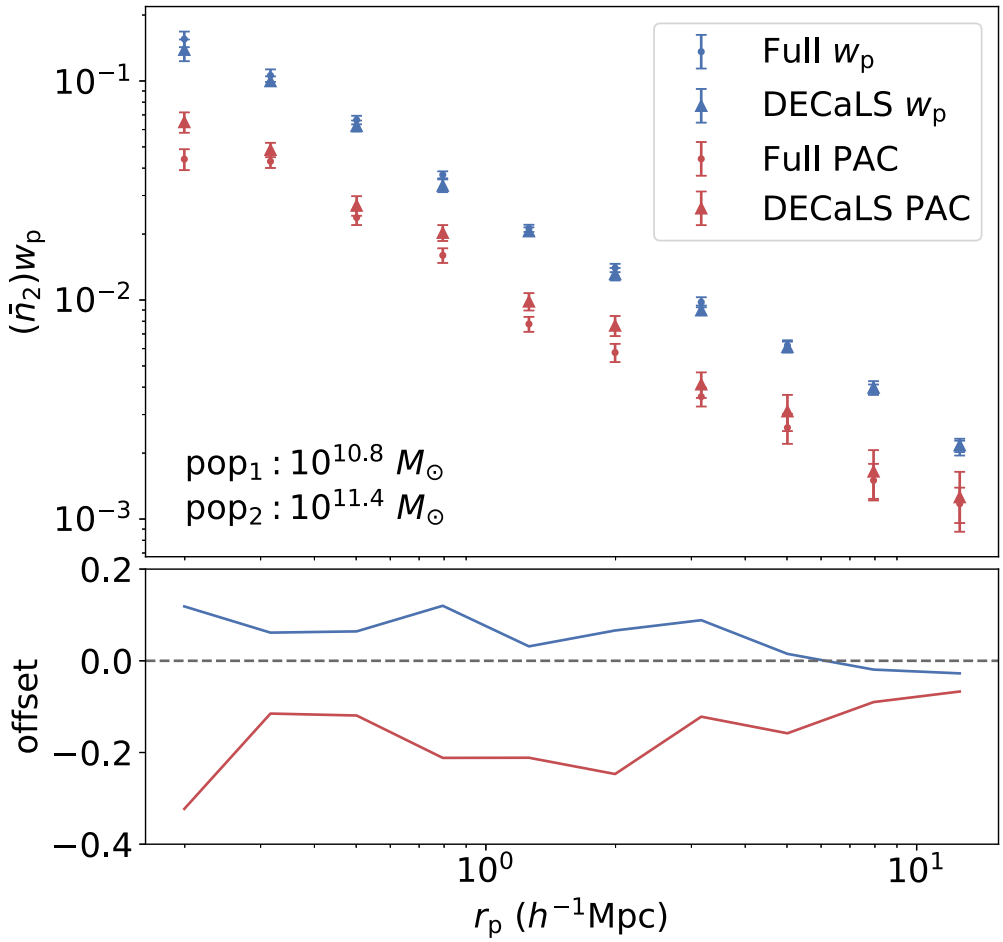

Figure C1. Comparing w_p (blue) and PAC $\bar{n}_2 w_p$ (red) measurements of the Full (DECaLS+BASS+MzLS) sample (dots) and DECaLS-only sample (triangles). The measurements are shown in the top panel, and the relative offsets of the Full sample from the DECaLS sample are shown in the bottom panel. The comparisons are for pop_1 with $10^{10.8}\,M_\odot$ and pop_2 with $10^{11.4}\,M_\odot$ at $z_s < 0.2$. w_p is divided by 5000 for better comparison.

ORCID iDs

Kun Xu https://orcid.org/0000-0002-7697-3306
Y. P. Jing https://orcid.org/0000-0002-4534-3125

References

Abazajian, K., Adelman-McCarthy, J. K., Agüeros, M. A., et al. 2004, AJ, 128, 502
Abazajian, K. N., Adelman-McCarthy, J. K., Agüeros, M. A., et al. 2009, ApJS, 182, 543
Alam, S., Albareti, F. D., Allende Prieto, C., et al. 2015, ApJS, 219, 12
Baldry, I. K., Driver, S. P., Loveday, J., et al. 2012, MNRAS, 421, 621
Baldry, I. K., Glazebrook, K., & Driver, S. P. 2008, MNRAS, 388, 945
Behroozi, P. S., Wechsler, R. H., & Conroy, C. 2013, ApJ, 770, 57
Bell, E. F., McIntosh, D. H., Katz, N., & Weinberg, M. D. 2003, ApJS, 149, 289
Bellstedt, S., Driver, S. P., Robotham, A. S. G., et al. 2020, MNRAS, 496, 3235
Benson, A. J. 2012, NewA, 17, 175
Blanton, M. R., Hogg, D. W., Bahcall, N. A., et al. 2003, ApJ, 592, 819
Blanton, M. R., & Roweis, S. 2007, AJ, 133, 734
Boquien, M., Burgarella, D., Roehlly, Y., et al. 2019, A&A, 622, A103
Bruzual, G., & Charlot, S. 2003, MNRAS, 344, 1000
Calzetti, D., Armus, L., Bohlin, R. C., et al. 2000, ApJ, 533, 682
Chabrier, G. 2003, PASP, 115, 763
Coil, A. L., Blanton, M. R., Burles, S. M., et al. 2011, ApJ, 741, 8
Cole, S., Norberg, P., Baugh, C. M., et al. 2001, MNRAS, 326, 255
Colless, M., Dalton, G., Maddox, S., et al. 2001, MNRAS, 328, 1039
Dark Energy Survey Collaboration, Abbott, T., Abdalla, F. B., et al. 2016, MNRAS, 460, 1270
Davé, R., Anglés-Alcázar, D., Narayanan, D., et al. 2019, MNRAS, 486, 2827
Davidzon, I., Bolzonella, M., Coupon, J., et al. 2013, A&A, 558, A23
Davidzon, I., Ilbert, O., Laigle, C., et al. 2017, A&A, 605, A70
Davis, M., Faber, S. M., Newman, J., et al. 2003, Proc. SPIE, 4834, 161
DESI Collaboration, Aghamousa, A., Aguilar, J., et al. 2016, arXiv:1611.00036
Desjacques, V., Jeong, D., & Schmidt, F. 2018, PhR, 733, 1
Dey, A., Schlegel, D. J., Lang, D., et al. 2019, AJ, 157, 168
Driver, S. P., Bellstedt, S., Robotham, A. S. G., et al. 2022, MNRAS, 513, 439
Driver, S. P., Hill, D. T., Kelvin, L. S., et al. 2011, MNRAS, 413, 971
Drory, N., Bundy, K., Leauthaud, A., et al. 2009, ApJ, 707, 1595
Eisenstein, D. J., Annis, J., Gunn, J. E., et al. 2001, AJ, 122, 2267
Faber, S. M., Willmer, C. N. A., Wolf, C., et al. 2007, ApJ, 665, 265
Fontana, A., Salimbeni, S., Grazian, A., et al. 2006, A&A, 459, 745
Foreman-Mackey, D., Hogg, D. W., Lang, D., & Goodman, J. 2013, PASP, 125, 306
Gao, H., Jing, Y. P., Zheng, Y., & Xu, K. 2022, ApJ, 928, 10
Garilli, B., Guzzo, L., Scodeggio, M., et al. 2014, A&A, 562, A23
Guo, H., Yang, X., & Lu, Y. 2018, ApJ, 858, 30
Henriques, B. M. B., Yates, R. M., Fu, J., et al. 2020, MNRAS, 491, 5795
Ilbert, O., McCracken, H. J., Le Fèvre, O., et al. 2013, A&A, 556, A55
Ivezić, Ž., Kahn, S. M., Tyson, J. A., et al. 2019, ApJ, 873, 111
Jing, Y. P. 1998, ApJL, 503, L9
Kinney, A. L., Calzetti, D., Bohlin, R. C., et al. 1996, ApJ, 467, 38
Kuijken, K., Heymans, C., Dvornik, A., et al. 2019, A&A, 625, A2
Landy, S. D., & Szalay, A. S. 1993, ApJ, 412, 64
Lang, D., Hogg, D. W., & Mykytyn, D. 2016, The Tractor: Probabilistic astronomical source detection and measurement, Astrophysics Source Code Library, ascl:1604.008
Laureijs, R., Amiaux, J., Arduini, S., et al. 2011, arXiv:1110.3193
Le Fèvre, O., Vettolani, G., Garilli, B., et al. 2005, A&A, 439, 845
Leauthaud, A., Bundy, K., Saito, S., et al. 2016, MNRAS, 457, 4021
Leja, J., Speagle, J. S., Johnson, B. D., et al. 2020, ApJ, 893, 111
Li, C., Kauffmann, G., Jing, Y. P., et al. 2006, MNRAS, 368, 21
Li, C., & White, S. D. M. 2009, MNRAS, 398, 2177
Lilly, S. J., Le Fèvre, O., Renzini, A., et al. 2007, ApJS, 172, 70
Maraston, C., Pforr, J., Henriques, B. M., et al. 2013, MNRAS, 435, 2764
McLeod, D. J., McLure, R. J., Dunlop, J. S., et al. 2021, MNRAS, 503, 4413
Mortlock, A., Conselice, C. J., Hartley, W. G., et al. 2015, MNRAS, 447, 2
Moster, B. P., Naab, T., & White, S. D. M. 2013, MNRAS, 428, 3121
Moustakas, J., Coil, A. L., Aird, J., et al. 2013, ApJ, 767, 50
Moutard, T., Arnouts, S., Ilbert, O., et al. 2016, A&A, 590, A102
Muzzin, A., Marchesini, D., Stefanon, M., et al. 2013, ApJ, 777, 18
Newman, J. A., & Gruen, D. 2022, ARA&A, 60, 363
Peacock, J. A., & Smith, R. E. 2000, MNRAS, 318, 1144
Peng, Y.-j., Lilly, S. J., Kovač, K., et al. 2010, ApJ, 721, 193
Petrosian, V. 1976, ApJL, 210, L53
Pillepich, A., Springel, V., Nelson, D., et al. 2018, MNRAS, 473, 4077
Popesso, P., Biviano, A., Böhringer, H., & Romaniello, M. 2006, A&A, 445, 29
Pozzetti, L., Bolzonella, M., Lamareille, F., et al. 2007, A&A, 474, 443
Pozzetti, L., Bolzonella, M., Zucca, E., et al. 2010, A&A, 523, A13
Reid, B., Ho, S., Padmanabhan, N., et al. 2016, MNRAS, 455, 1553
Rodríguez-Puebla, A., Avila-Reese, V., Yang, X., et al. 2015, ApJ, 799, 130
Schaye, J., Crain, R. A., Bower, R. G., et al. 2015, MNRAS, 446, 521
Schlegel, D. J., Finkbeiner, D. P., & Davis, M. 1998, ApJ, 500, 525
Shuntov, M., McCracken, H. J., Gavazzi, R., et al. 2022, A&A, 664, A61
Somerville, R. S., Hopkins, P. F., Cox, T. J., Robertson, B. E., & Hernquist, L. 2008, MNRAS, 391, 481
Tinker, J. L., Robertson, B. E., Kravtsov, A. V., et al. 2010, ApJ, 724, 878
Tomczak, A. R., Quadri, R. F., Tran, K.-V. H., et al. 2014, ApJ, 783, 85
Wang, L., & Jing, Y. P. 2010, MNRAS, 402, 1796
Wang, L., Li, C., Kauffmann, G., & De Lucia, G. 2006, MNRAS, 371, 537
Wang, W., Jing, Y. P., Li, C., Okumura, T., & Han, J. 2011, ApJ, 734, 88
Weigel, A. K., Schawinski, K., & Bruderer, C. 2016, MNRAS, 459, 2150
Wright, A. H., Driver, S. P., & Robotham, A. S. G. 2018, MNRAS, 480, 3491
Wright, E. L., Eisenhardt, P. R. M., Mainzer, A. K., et al. 2010, AJ, 140, 1868
Xu, K., & Jing, Y. 2022, ApJ, 926, 130
Xu, K., Zheng, Y., & Jing, Y. 2022, ApJ, 925, 31
Yang, X., Mo, H. J., van den Bosch, F. C., Zhang, Y., & Han, J. 2012, ApJ, 752, 41
York, D. G., Adelman, J., Anderson, J. E. J., et al. 2000, AJ, 120, 1579
Zhou, R., Newman, J. A., Dawson, K. S., et al. 2020, RNAAS, 4, 181
Zhou, R., Newman, J. A., Mao, Y.-Y., et al. 2021, MNRAS, 501, 3309
Zu, Y., & Mandelbaum, R. 2016, MNRAS, 457, 4360